The International Journal of Advanced Manufacturing Technology (2023) 129:2183–2193
https://doi.org/10.1007/s00170-023-12349-2

ORIGINAL ARTICLE

Realization of stretchable metasurface system with adaptive wettability using additive manufacturing

Hoo Min Lee[1] · Da Yeon Shin[1,2] · Gil Ho Yoon[1]

Received: 30 March 2023 / Accepted: 17 September 2023 / Published online: 12 October 2023

Abstract

This study aims to design a stretchable metasurface system that can adaptively change its wettability using additive manufacturing. The system consists of a stretchable specimen with micro-surface patterns and a bi-layer actuator based on compliant mechanisms. Both the specimen and actuator are manufactured using fused filament fabrication additive manufacturing methods. In the proposed system, the actuator stretches the specimen to modify the aspect ratios of the surface patterns. These changes in aspect ratios reduce the air gaps at the liquid/solid interface, which weakens the hydrophobic properties of the specimen surface. To investigate the effect of changes in pattern aspect ratios on surface wettability, experiment is conducted by dropping water droplets onto the specimen while the actuator stretches it. The contact angles of the droplets are measured to quantify the changes in wettability. Additionally, finite element simulations are performed to analyze the specimen strain distribution under various deformation conditions. This allows the evaluation of precise elongation values and prediction of surface wettability, displaying the potential for surface wettability control. These findings support the implementation of additive manufacturing to fabricate a stretchable metasurface system with adaptive wettability.

Keywords Adaptive wettability · Additive manufacturing · Stretchable metasurface · Micro-surface pattern · Compliant mechanism actuator

1 Introduction

This study aims to design a stretchable metasurface system with adaptive wettability using additive manufacturing. The system consists of a stretchable specimen with micro-surface patterns and a compliant mechanism-based actuator, both of which are manufactured using the fused filament fabrication method. In this system, the actuator stretches the specimen to modify the geometries of the surface patterns, which results in changes to the aspect ratios of the patterns. This reduces the air gaps at the liquid/solid interface and weakens the surface hydrophobicity. To investigate the relationship between surface wettability and specimen elongation length, experiment was conducted to measure the water contact angle (WCA). Additionally, finite element (FE) simulations were conducted to analyze the distribution of specimen strain under various deformation conditions. The experimental and simulation results were then used to predict the surface wettability for various specimen deformation cases in the present study.

Superhydrophobic surfaces are defined as surfaces with extreme hydrophobic characteristics, where the WCAs of droplets exceed 150° [1]. Many relevant studies regarding surface and interfacial phenomena have been conducted on superhydrophobic surfaces, demonstrating promising applications in engineering fields. These include the application of hydrophobic surfaces for various purposes such as spray retention [2], prevention of ice adhesion [3], anti-corrosion [4], and increased water protection [5]. Research has also been conducted on changing and controlling wettability for a variety of engineering applications. Relevant studies have been done on various types of surfaces [6–9] and applied in various engineering applications such as magneto-switchable electrodes [10], smart packaging [11], fluidic

✉ Gil Ho Yoon
gilho.yoon@gmail.com

Hoo Min Lee
hoominlee95@gmail.com

Da Yeon Shin
tlsekdus95@gmail.com

[1] Department of Mechanical Engineering, Hanyang University, Seoul 04763, South Korea

[2] Department of Research and Development, LG Innotek, Seoul 07796, South Korea

system transport [12], and biomedical implant purposes [13]. To enhance wettability control efficiency, studies have been conducted on the effects of chemical composition [14–16], surface micro-structures [17–20], and nanomaterials [21] on the wettability of surfaces. Investigation of factors affecting interfacial phenomena have also been conducted in [22, 23]. Based on these studies, various methods have been proposed in the engineering fields to fabricate functional hydrophobic surfaces using chemical vapor deposition [24–26], laser processing [27–29], and solution approach methods [30]. However, these proposed methods involve expensive equipment and can lead to structural damage to fabricated surfaces. Therefore, additive manufacturing has gained popularity in the fields of wettability control and fabrication of functional hydrophobic surfaces. Studies have been conducted to investigate the effects of layer heights [31] and printing angles [32] on the surface roughness of additive manufactured products. These studies have led to the realization of functional surfaces with wettability gradient by modifying the surface roughness [33]. While significant progress has been achieved in realizing surfaces with different wetness levels on a single functional surface, there were limitations in actively controlling surface wettability. Thus, the present study aims to overcome these limitations and develop a system where the wettability of fabricated functional surfaces is actively controlled through the variation of micro-surface patterns using actuators. To fully utilize the rapid additive manufacturing scheme, the idea of compliant mechanism-based additive manufactured actuators [34, 35] is utilized in the proposed method to actively control surface wettability.

The present research aims to use additive manufacturing to design a stretchable metasurface system that realizes adaptive wettability. The system comprises a stretchable specimen with micro-surface patterns and a compliant mechanism-based actuator. The specimen was made of silicone rubber and fabricated using a polylactic acid (PLA) plastic mold manufactured using the fused filament fabrication method. Liquid silicone and a curing agent were poured into the mold and detached after the curing process was over to finalize the silicone rubber specimens with micro-surface patterns. The valley region (i.e., the area between individual pattern structures) represents the part where the PLA mold existed. This surface feature provides the most sufficient air gaps at the liquid/solid interface and helps water droplets slide readily [36], thereby strengthening the surface hydrophobicity. This property is weakened when the patterns are deformed to have lower aspect ratios, thus reducing the volume of valley regions and the air gaps at the interface. In the proposed system, this mechanism was realized by stretching the specimen to reduce the pattern angle, as illustrated in Fig. 1. The elongation of the specimen was carried out using the compliant mechanism-based actuator. The actuator was designed based on compliant mechanism topologies and manufactured

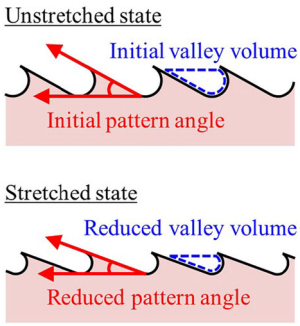

Fig. 1 Mechanism of stretchable metasurface with adaptive wettability

using the fused filament fabrication method. The relationship between the surface wettability and the specimen elongation length was investigated using the WCA measurement experiment. Furthermore, FE simulations were conducted to analyze specimen strain distribution and evaluate elongation values for different cases of specimen deformation. Together with the experimental results, this made it possible to predict and control the surface wettability under different deformation conditions. This feature could be utilized in future applications such as self-draining coatings for solar panels [37] and functional windows [38] by enabling drainage channels that are highly hydrophobic compared to other parts of the coated surface. The presented study supports the implementation of additive manufacturing for the fabrication of a stretchable metasurface system with adaptive wettability.

The remainder of this paper is organized as follows. Section 2 provides the problem definition and optimal design of compliant mechanism topologies. Section 3 provides the explanation on system manufacturing and wettability testing method. In Section 4, the results of the proposed system's changing wettability are presented and discussed. Section 5 presents further studies done for wettability prediction and control using FE simulations. Conclusion and future research topics are discussed in Section 6.

2 Optimization of compliant mechanism

2.1 Optimization formulation

The terms SE (strain energy) and MSE (mutual strain energy) are used in the general design of the traditional spring model for elastic structures that include compliant mechanisms. SE and MSE describe the stiffness and flexibility of the designed mechanism, respectively [39]. SE and MSE are formulated as follows:

$$\mathrm{SE} = \frac{1}{2}\int_A \sigma_1^{\mathrm{T}} \varepsilon_1 dA \tag{1}$$

$$\text{MSE} = \int_A \sigma_2^{\mathrm{T}} \varepsilon_1 dA \tag{2}$$

where σ_1, σ_2, ε_1, and A are the stress vector produced by the input force, stress vector produced by the unit virtual force, strain vector produced by input force, and the design area. In topology optimization, the design domain is divided into elements using the finite element method, making it possible to calculate SE and MSE numerically. The displacement vector $\mathbf{U}$ due to input force and the displacement vector $\mathbf{V}$ due to unit virtual force can be achieved as follows:

$$\mathbf{KU} = \mathbf{F}, \quad \mathbf{KV} = \mathbf{F}_{\mathrm{v}} \tag{3}$$

where $\mathbf{K}$, $\mathbf{F}$, and $\mathbf{F}_{\mathrm{v}}$ are the global stiffness matrix of the design domain, load vector with the input load, and the load vector with the unit virtual load. With the displacement fields, it is possible to calculate the SE and MSE as follows:

$$\text{SE} = \frac{1}{2}\mathbf{U}^{\mathrm{T}}\mathbf{KU}, \quad \text{MSE} = \mathbf{V}^{\mathrm{T}}\mathbf{KU} \tag{4}$$

The present optimization aims to maximize the output displacement ϕ at a desired node. The output displacement can be formulated using SE and MSE as follows:

$$\phi = \mathbf{F}_{\mathrm{v}}^{\mathrm{T}}\mathbf{U} = \mathbf{V}^{\mathrm{T}}\mathbf{KU} = \text{MSE} \tag{5}$$

In [40], various objective functions were proposed for optimizing compliant mechanism design. Out of these, the objective function that focused on maximizing the output displacement was chosen as the representative one. Thus, the objective function was defined as follows:

$$\begin{aligned} &\underset{\mathbf{x}}{\text{Max}} : \phi(\mathbf{x}) = \mathbf{V}^{\mathrm{T}}\mathbf{KU} = \sum_{e=1}^{N} (x_e)^p \mathbf{V}_e^{\mathrm{T}} \mathbf{K}_e \mathbf{U}_e \\ &\text{Subject to} : \frac{V(\mathbf{x})}{V_o} = f, \ \mathbf{KU} = \mathbf{F}, \ 0 \le \mathbf{x} \le 1 \end{aligned} \tag{6}$$

where $\mathbf{x}$, N, x_e, p, $\mathbf{V}_e$, $\mathbf{K}_e$, and $\mathbf{U}_e$ are the density vector, number of elements, density values at each element, penalization factor, element displacement vector due to unit virtual load, stiffness matrix, and element displacement vector due to input load, respectively. The material volume, design domain volume, and volume fraction are expressed as $V(\mathbf{x})$, V_0, and f, respectively.

2.2 Sensitivity analysis

The optimization problem was solved using the optimality criteria (OC) method. Due to the large number of design variables, the adjoint method was pursued to perform the sensitivity analysis. The sensitivity of Eq. 5 with respect to x_e was derived by introducing the following augmented function:

$$\tilde{\phi} = \mathbf{V}^{\mathrm{T}}\mathbf{KU} + \lambda_1^{\mathrm{T}}(\mathbf{KU} - \mathbf{F}) + \lambda_2^{\mathrm{T}}(\mathbf{KV} - \mathbf{F}_{\mathrm{v}}) \tag{7}$$

where λ_1 and λ_2 are the adjoint vectors. Note that this augmented function is equal to the original function as the terms $(\mathbf{KU} - \mathbf{F})$ and $(\mathbf{KV} - \mathbf{F}_{\mathrm{v}})$ are equal to zero, as shown in Eq. 3. Differentiation of $\tilde{\phi}$ and rearranging of the terms result in the following equation:

$$\begin{aligned} \frac{\partial \tilde{\phi}}{\partial x_e} =& \frac{\partial \mathbf{U}}{\partial x_e}(\mathbf{KV} + \mathbf{K}\lambda_1) + \frac{\partial \mathbf{V}}{\partial x_e}(\mathbf{KU} + \mathbf{K}\lambda_2) \\ &+ \mathbf{V}^{\mathrm{T}}\frac{\partial \mathbf{K}}{\partial x_e}\mathbf{U} + \lambda_1^{\mathrm{T}}\frac{\partial \mathbf{K}}{\partial x_e}\mathbf{U} + \lambda_2^{\mathrm{T}}\frac{\partial \mathbf{K}}{\partial x_e}\mathbf{V} \end{aligned} \tag{8}$$

To eliminate the implicit derivatives $\frac{\partial \mathbf{U}}{\partial x_e}$ and $\frac{\partial \mathbf{V}}{\partial x_e}$, adjoint vectors λ_1 and λ_2 are defined as follows:

$$\lambda_1 = -\mathbf{V}, \quad \lambda_2 = -\mathbf{U} \tag{9}$$

The defined adjoint vectors allow the simplification of Eq. 8 as follows:

$$\frac{\partial \tilde{\phi}}{\partial x_e} = -\mathbf{V}^{\mathrm{T}}\frac{\partial \mathbf{K}}{\partial x_e}\mathbf{U} \tag{10}$$

Taken into account that $\mathbf{K}$ can be expressed in terms of $\mathbf{K}_e$ and p, $\frac{\partial \mathbf{K}}{\partial x_e}$ can be expressed as follows:

$$\frac{\partial \mathbf{K}}{\partial x_e} = p(x_e)^{p-1}\mathbf{K}_e \tag{11}$$

Thus, the sensitivity of objective function ϕ with respect to x_e can be computed as follows:

$$\frac{\partial \phi}{\partial x_e} = -p(x_e)^{p-1}\mathbf{V}_e^{\mathrm{T}}\mathbf{K}_e\mathbf{U}_e \tag{12}$$

Using this equation and the OC method, sensitivity analysis was done to obtain the optimal design for the compliant mechanism-based actuator.

2.3 Design parametrization

The design parameters for the compliant mechanism-based actuator were defined based on the optimization formulation, as shown in Fig. 2. The actuator is designed to convert forces applied at the input ports to an output displacement at the two output ports in a direction orthogonal to the force vectors. For simplicity, symmetry was considered for this problem. In the

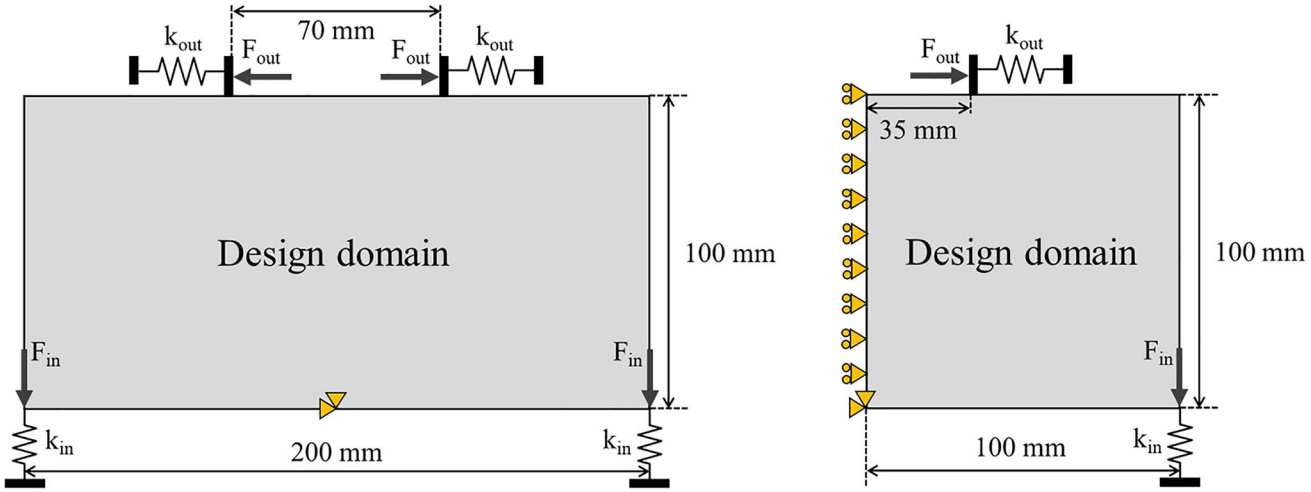

Fig. 2 The problem definition and the simplified definition of compliant mechanism-based actuator

simplified problem, the design domain is a square with a width and height of 100 mm. The input and output ports are located at the right end node of the lower boundary and at the upper boundary 35 mm away from the left end, respectively. The restricted degrees of freedom are positioned at the left end of the lower boundary. The domain was discretized using 100 × 100 square elements with an edge length of 1.0 mm. The objective volume fraction, filter radius, penalization factor, and convergence value were set as 0.3, 1.5 mm, 3, and 1.0×10^{-4}, respectively.

Figure 3 illustrates the result of the topology optimization for the prescribed stiffness of the input spring (k_{in}=1) and the stiffness of output spring (k_{out}=0.001). These stiffness values were selected to account for the difference in stiffness between the rigid actuator body and the silicone rubber specimen. Convergence was achieved at the 778th iteration, as the changes in design variables became smaller than the predefined convergence value. The result of the simplified problem could be used to obtain the result of the initial optimization problem and to determine the total geometry of the compliant mechanism-based actuator. The designed actuator consists of two hinges, each of which serves to change the direction of the force vector F_{in} and produce output displacements in orthogonal directions.

3 Experimental section

3.1 Stretchable specimen fabrication

The stretchable specimen was fabricated using a 3D-printed PLA plastic mold, which was designed using computer-aided design software and printed using the fused filament fabrication method with a Dremel Digilab 3D45 printer. The printing

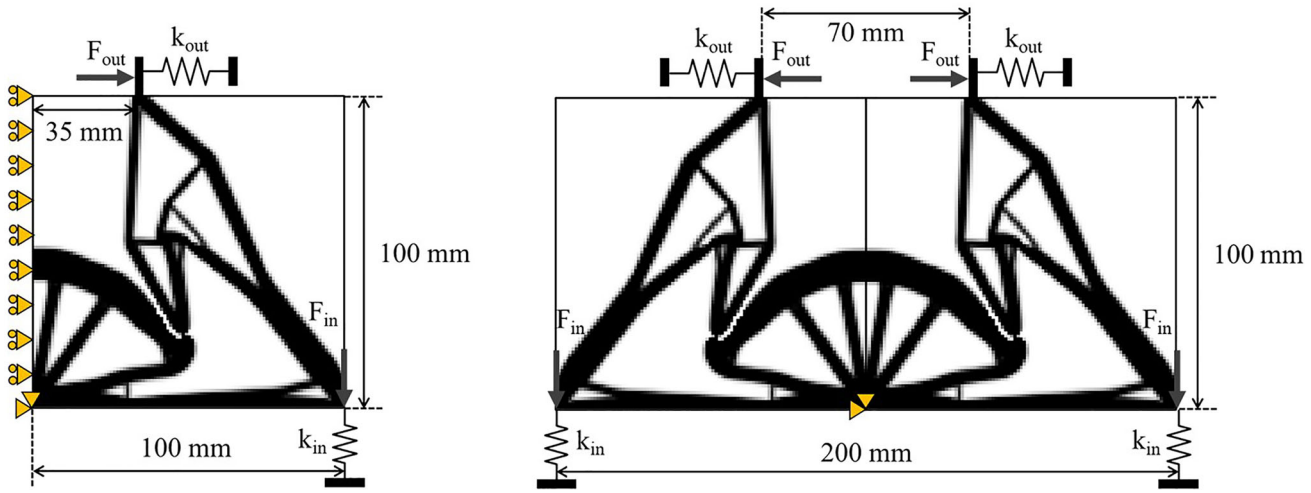

Fig. 3 The solution of the simplified problem and the full solution of compliant mechanism-based actuator

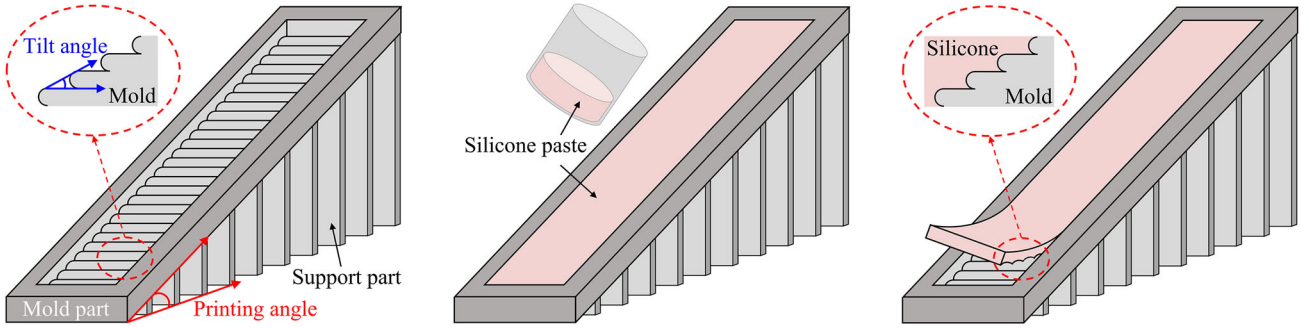

a. Manufacturing PLA mold on support parts by additive manufacturing

b. Pouring silicone paste into the printed mold and drying at room temperature for 2 hours

c. Realization of surface patterns on specimen after the detachment process

Fig. 4 Manufacture process of stretchable specimen with micro-surface patterns

speed, extruder temperature, platform temperature, and infill density were set to 50 mm/s, 200 °C, 50 °C, and 20%, respectively. The eSUN PLA 3D printer filament with a diameter of 1.75 mm was used to print the molds, with a layer height of 0.30 mm. It is important to note that PLA is printed in circular tube shapes and that the mold was printed on support parts at a printing angle of 30°. The stacking of circular PLA tubes and the printing angle induced the surface of the PLA molds to have a continuous arch-shaped geometry, with a tilt angle of 30°.

After the mold manufacture process, Jnmade S1 liquid silicone and curing agent (20:1 ratio) were mixed and poured into the printed mold to create the stretchable specimen. The silicone paste was allowed to cure at room temperature for 2 h before being detached from the mold. Raising the curing temperature can decrease the curing time and hence speed up the manufacture process, but additional treatment might be required to separate the specimen afterward. The specimen was designed to have length, width, and thickness values of 100 mm, 20 mm, and 2 mm, respectively. Two holes with length, width, and depth of 5 mm, 3 mm, and 1.5 mm were created on the bottom of the specimen to allow attachment with the actuator. The arch-shaped geometry of the mold surface induced the detached specimen to have continuous wave-shaped micro-surface pattern with pattern angle of 30°, identical to the value of tilt angle. The specimen fabrication process and the specimen surface pattern realization mechanism are illustrated in Fig. 4. The manufactured specimen and the magnified image of its micro-surface patterns are shown in Fig. 5.

3.2 Actuator manufacturing

The actuator was designed using computer-aided design software based on the topology optimization results in Section 2. The actuator was printed using the Flashforge Dreamer 3D printer with dual extruders shown in Fig. 6a. The printing speed, platform temperature, and infill density were set as 20 mm/s, 100 °C, and 100%, respectively. Two materials were used in the manufacture process to achieve high stiffness while realizing hinges that facilitate bending. The materials used are shown in Fig. 6b: a rigid acrylonitrile butadiene styrene (ABS) plastic was used for the actuator body, while a flexible thermoplastic polyurethane (TPU) was used for the hinges. The Flashforge ABS filament and the eSUN TPU filament, both having a diameter of 1.75 mm, were used in the additive manufacture process with 240 °C and 205 °C extruding temperatures, respectively. The layer heights of the printed ABS and TPU were set as 0.200 mm. The printed bi-layer compliant mechanism-based actuator is shown in Fig. 6c.

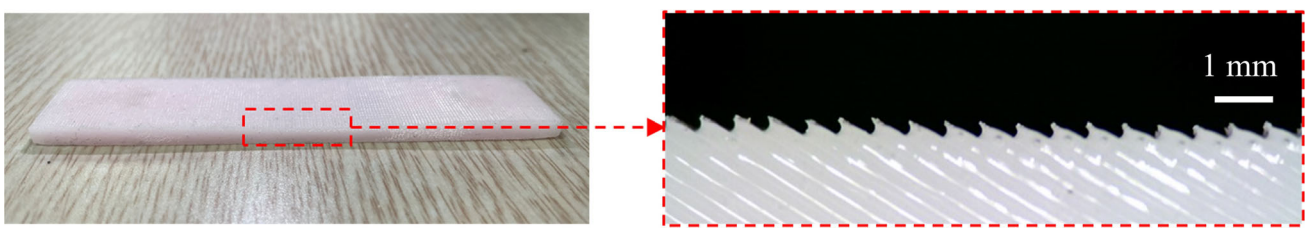

Fig. 5 Manufactured specimen with micro-surface patterns

Fig. 6 **a** 3D printer used to print the bi-layer actuator, **b** ABS and TPU filaments used for the bi-layer actuator, and **c** printed bi-layer compliant mechanism-based actuator

3.3 Testing and characterization

Experiment was conducted to investigate the change in specimen surface wettability when stretched by the actuator. WCAs of water droplets dropped on the specimen were measured for different cases of elongation length. The experimental setup is shown in Fig. 7. The actuator was fixed using a jig, and the specimen was attached to the actuator by fitting the top parts of the actuator into the bottom holes of the specimen. Masses of equal weights (100 g) were added to each end of the actuator for every trial the specimen was stretched. For each trial, water droplets were dropped on the center of the specimen to measure the WCAs. Micro-pipette was utilized in this process to ensure that droplets with constant volume of 3.5 μl were dropped on the specimen. ViTiny UM12 digital microscope was used to acquire enlarged images of surface patterns and water droplets. The microscope was set to a magnification of 32× for precise measurement of the surface pattern and WCAs. Various relations between added mass, elongated length, pattern angle, and WCA were investigated to evaluate the changes in specimen surface wettability.

4 Results and discussion

An experiment was first conducted to investigate the performance of the actuator in stretching the specimen. The relation between the mass added to the actuator and the resulting elongation length of the specimen was analyzed. This experimental result is presented in Fig. 8. The result shows the mean value of 10 experiments, each conducted using different stretchable specimen. Note that the experiment was done by applying equal masses to each end of the actuator, until the elongation length value reached approximately 10 mm to

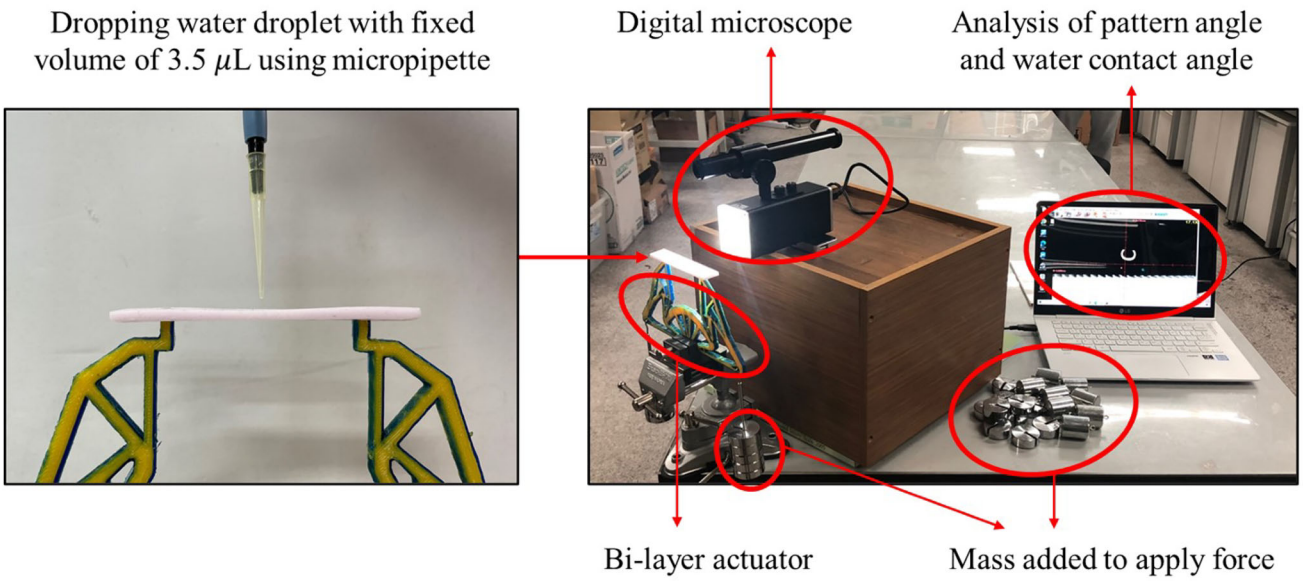

Fig. 7 Experimental setup to measure changes in pattern angles and water contact angles

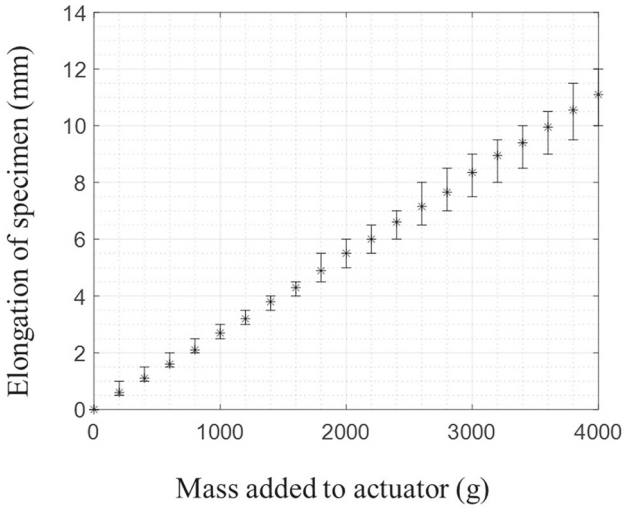

Fig. 8 Experiment results. Relation between mass and elongation of specimen

only consider elastic deformation. The experiment was conducted with a maximum load of 4000 g, with 2000 g applied to each end of the actuator. The average elongation length of the specimen at a load of 4000 g was 11.1 mm. The results suggest a linear relationship between added mass and elongation length, where the average load needed to elongate the specimen by 1.0 mm is 360.36 g.

The following experiment was conducted to investigate the system's adaptive wettability features with changing specimen elongation values. A total of 10 experiments were conducted using different specimens, and the mean value was used for the analysis. Figure 9a presents the relation between specimen elongation and pattern tilt angle. The mean pattern angle changed from 30.14 to 20.23° as the specimen was elongated by 10 mm from its initial state, showing a total reduction of 9.91°. Figure 9b presents the relation between specimen elongation and WCA. The mean WCA reduced from 136.78 to 122.69° when the specimen was elongated by 10 mm from its initial state. This reduction in WCA by 14.09° demonstrates that the stretchable metasurface system, incorporating micro-surface patterns and compliant mechanism-based actuators, is capable of exhibiting adaptive wettability. The mean changes in load applied to actuator, pattern angle, and WCA for specimen elongation of 10 mm are summarized in Table 1.

Table 1 Mean changes in parameters for elongation length 10 mm

Load (g)	Pattern angle (°)	Water contact angle (°)
3603.6	−9.91	−14.09

5 Wettability prediction

The significance of the elongation–WCA relationship presented in Fig. 9b lies not only in demonstrating the adaptive wettability characteristics of the system but also in highlighting its potential for wettability control. Each elongation value of the specimen corresponds to a specific WCA. This suggests that it is possible to control surface wettability by inducing specific elongation values in the specimen. To verify the potential for wettability control, we predicted WCAs

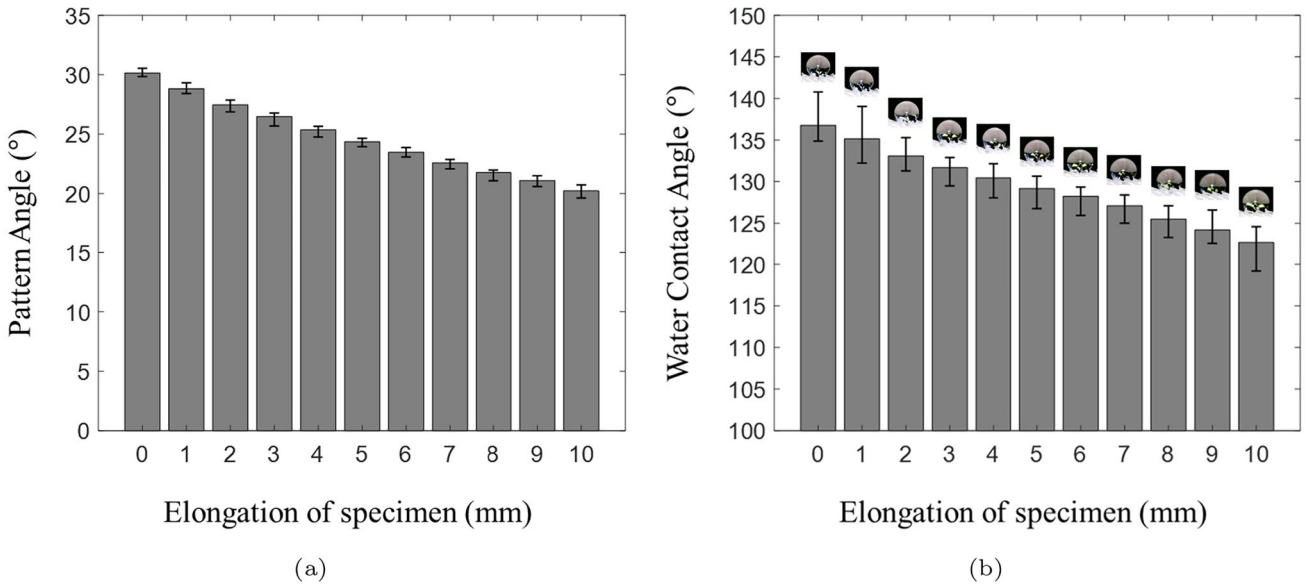

Fig. 9 Experiment results. **a** Relation between elongation of specimen and pattern tilt angle and **b** relation between elongation of specimen and WCA

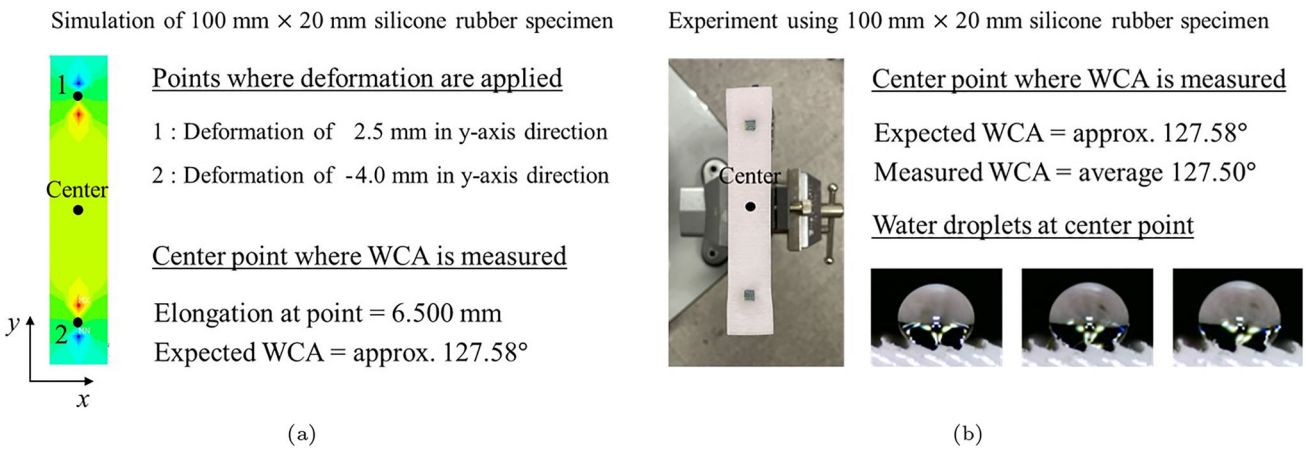

Fig. 10 **a** Simulation results of stretchable specimen and **b** experimental results of stretchable specimen

using strain distributions simulated through FE analysis and the elongation–WCA relationship. These predictions were then experimentally validated by measuring the actual WCAs under identical deformation conditions.

ANSYS Mechanical APDL 2021 R2 was used to analyze the strain distributions of stretchable specimens under various deformation conditions. The specimen was discretized using SHELL 63 four-node quadrilateral shell elements, with each element having a constant length and width of 4 mm. The material properties were defined with Young's modulus of 3.4 MPa and Poisson's ratio of 0.35. Note that the aim of the FE simulation is to evaluate the precise elongation values at different points of the specimen to predict surface wettability using the specimen elongation–WCA relation. Thus, surface properties were not realized in the FE simulation process.

The first case study considered a specimen of the same size as the one used in the experiment, modeled using 125 elements. In contrast to the experiments where identical masses were used to create equal deformations in opposite directions, deformations of 2.5 mm and 4.0 mm in opposing directions were applied to introduce varying deformation magnitudes at each point. The tensile strain of the specimen at center point was analyzed to predict the corresponding WCA. The simulation conditions and results are shown in Fig. 10a, which indicates that the elongation at the center point is 6.5 mm. Based on the experimental result of the elongation–WCA relation, the expected WCA is approximately 127.58°.

Experiment was conducted to validate the predicted WCA value for the first case study. Masses of 900 g and 1350 g were applied to each end of the actuator to induce deformations of 2.5 mm and 4.0 mm in opposing directions. A water droplet of 3.5 μl was dropped on the center of the specimen, and ten experiments were conducted to acquire the mean WCA of the water droplets. The results of the experiments are shown in Fig. 10b, which reveals that the mean WCA is 127.50°. The predicted and measured WCAs have a small difference of 0.08°, indicating that the prediction of surface wettability shows great accuracy.

The second case study considered a larger specimen with a length of 100 mm, width of 100 mm, and thickness of

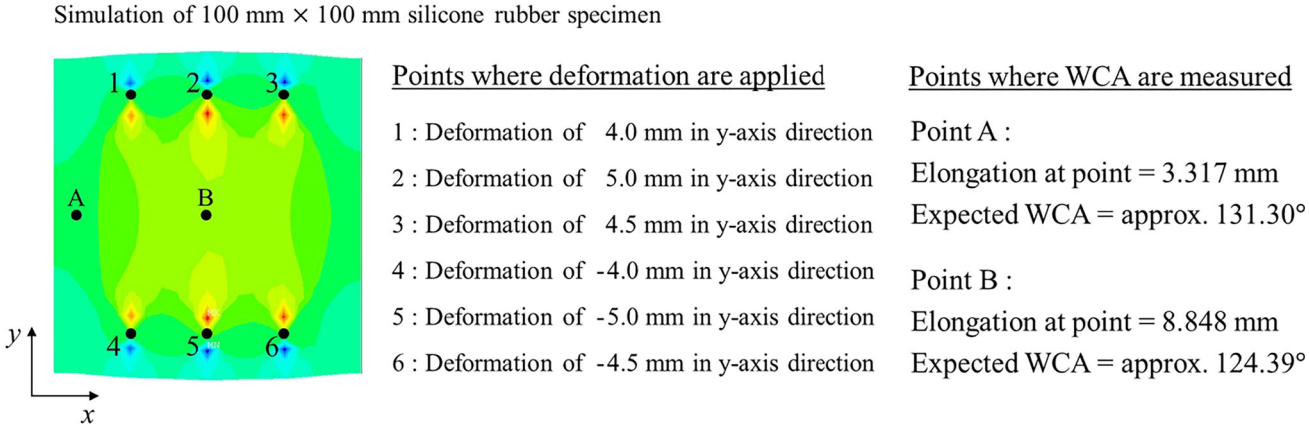

Fig. 11 Simulation results of stretchable specimen using three actuators

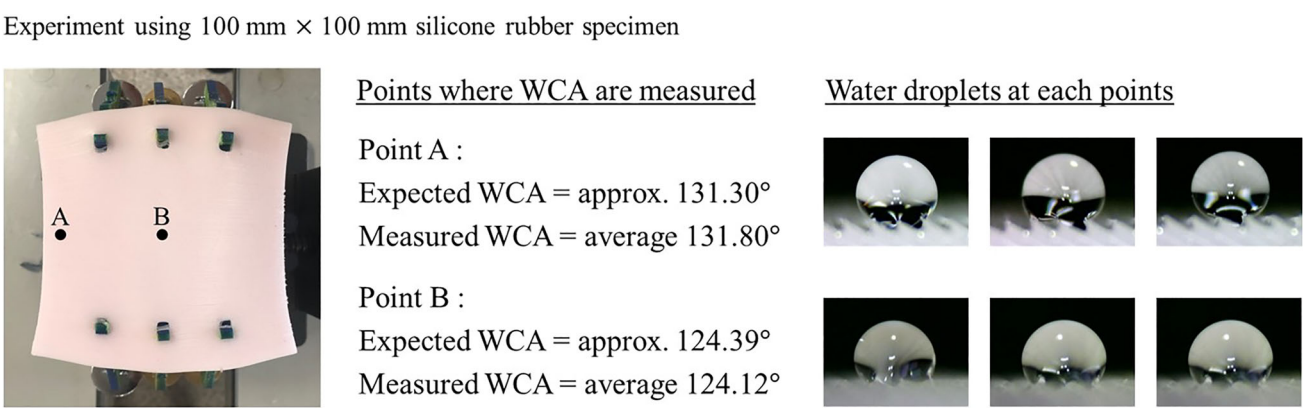

Fig. 12 Experimental results of stretchable specimen using three actuators

2 mm. The specimen was modeled using 625 elements. The simulation conditions and results are presented in Fig. 11. Deformations of 4.0 mm, 4.5 mm, and 5.0 mm were considered to diversify the strain distribution. Two points A and B were defined to be located near the edge and in the middle of the specimen, respectively. The tensile strain distribution of the specimen was analyzed to predict the WCAs at these specific points. The results show that the elongation values are 3.317 mm and 8.848 mm at points A and B, respectively. Using the elongation–WCA relation, we could evaluate that the expected WCA values are 131.30° and 124.39° at points A and B, respectively. We can infer from the results that the edge of the specimen experienced smaller elongation, resulting in greater surface hydrophobicity compared to the center of the specimen.

Experiment was conducted to validate the predicted WCA values at points A and B. A new PLA mold was manufactured using the Dremel Digilab 3D45 printer. The mold was used to fabricate stretchable specimens with six holes to allow attachment with three actuators simultaneously. Masses of 1500 g, 1650 g, and 1800 g were applied to the ends of each actuator to induce the desired deformation values of 4.0 mm, 4.5 mm, and 5.0 mm. Water droplets of 3.5 μl were dropped on the designated points of the specimen, and ten experiments were conducted to acquire the mean WCAs. The results are presented in Fig. 12. The measured mean WCA values are 131.80° and 124.12° at points A and B, respectively. The predicted and measured WCAs at points A and B differed only slightly with differences of 0.50° and 0.27°, respectively. Despite the variation in elongation and WCA values at two different parts of the specimen, the method using FE simulation and experimental elongation–WCA relation demonstrated high accuracy of predicting surface wettability. These findings support the proposed stretchable metasurface system with adaptive wettability as a means of predicting and controlling surface wettability under various deformation conditions.

6 Conclusion

This study realizes stretchable metasurface system with adaptive wettability using a stretchable specimen with micro-surface patterns and compliant mechanism-based actuator. The actuator design incorporates compliant mechanism topology to maximize the efficiency of converting downward forces into horizontal displacements for specimen stretching. Both the metasurface of the stretchable specimen and the rigid-flexible actuator were fabricated using additive manufacturing, respectively, by incorporating geometric imperfections caused by printing in the form of circular tubes and the capability to blend two printing materials during the manufacturing process. Experiments were conducted to investigate the adaptive wettability feature of the manufactured system, which involved measuring the pattern angles of surface patterns and WCAs of water droplets dropped on the stretched specimen. The experiment validated that the stretching of the specimen induced changes in micro-surface pattern geometry and WCAs, with an average reduction of 9.91° and 14.09°, respectively, at an elongation length of 10 mm. Extended studies were conducted to predict surface wettability based on FE simulations of strain distribution at different deformation conditions. The simulated strain distribution allowed for the precise evaluation of specimen elongation at different points, enabling the prediction of WCAs at those exact points based on experimental data of the specimen elongation–WCA relation. Case studies involving experimental validations were conducted for verification, and the differences between predicted and measured WCAs were small, with values being 0.08°, 0.50°, and 0.27°. Overall, this research demonstrates the use of additive manufacturing to realize a stretchable metasurface system with adaptive wettability. The introduction of compliant mechanism-based actuators has overcome the limitations in actively controlling surface wettability that were found in previous work on functional surfaces. However, more research is required to make

this system usable in real-world engineering applications. For future research, the optimization of pattern angles and strain distribution within specimens, taken into consideration delicate drainage processes, can be conducted to address practical issues.

Author Contributions All authors contributed to the study conception and design. Material preparation, data collection, and analysis were performed by HML, DYS, and GHY. The first draft of the manuscript was written by HML, and all authors commented on previous versions of the manuscript. All authors read and approved the final manuscript.

Funding This work was supported by Korea Institute of Energy Technology Evaluation and Planning (KETEP) grant funded by the Korea government (MOTIE) (20202020800030, Development of Smart Hybrid Envelope Systems for Zero Energy Buildings through Holistic Performace Test and Evaluation Methods and Fields Verifications).

Declarations

Competing interests The authors declare no competing interests.

References

1. Ma M, Hill RM (2006) Superhydrophobic surfaces. Curr Opin Colloid Interface Sci 11(4):193–202
2. Massinon M, Lebeau F (2012) Experimental method for the assessment of agricultural spray retention based on high-speed imaging of drop impact on a synthetic superhydrophobic surface. Biosys Eng 112(1):56–64
3. Tong W, Xiong D, Wang N, Wu Z, Zhou H (2019) Mechanically robust superhydrophobic coating for aeronautical composite against ice accretion and ice adhesion. Compos B Eng 176: 107267
4. Zhang B, Xu W, Zhu Q, Yuan S, Li Y (2019) Lotus-inspired multiscale superhydrophobic AA5083 resisting surface contamination and marine corrosion attack. Materials 12(10):1592
5. Karmouch R, Ross G (2010) Superhydrophobic wind turbine blade surfaces obtained by a simple deposition of silica nanoparticles embedded in epoxy. Appl Surf Sci 257(3):665–669
6. Watanabe T (2009) Wettability of ceramic surfaces-a wide range control of surface wettability from super hydrophilicity to super hydrophobicity, from static wettability to dynamic wettability. J Ceram Soc Jpn 117(1372):1285–1292
7. Zhou Y, Wang B, Song X, Li E, Li G, Zhao S, Yan H (2006) Control over the wettability of amorphous carbon films in a large range from hydrophilicity to super-hydrophobicity. Appl Surf Sci 253(5):2690–2694
8. Piferi C, Bazaka K, D' Aversa D, Di Girolamo R, De Rosa C, Roman HE, Riccardi C, Levchenko I (2021) Hydrophilicity and hydrophobicity control of plasma-treated surfaces via fractal parameters. Adv Mater Interfaces 8(19):2100724
9. Jankauskaitė V, Narmontas P, Lazauskas A (2019) Control of polydimethylsiloxane surface hydrophobicity by plasma polymerized hexamethyldisilazane deposition. Coatings 9(1):36
10. Katz E, Sheeney-Haj-Ichia L, Basnar B, Felner I, Willner I (2004) Magnetoswitchable controlled hydrophilicity/hydrophobicity of electrode surfaces using alkyl-chain-functionalized magnetic particles: Application for switchable electrochemistry. Langmuir 20(22):9714–9719
11. Samyn P (2013) Wetting and hydrophobic modification of cellulose surfaces for paper applications. J Mater Sci 48(19):6455–6498
12. Tenjimbayashi M, Higashi M, Yamazaki T, Takenaka I, Matsubayashi T, Moriya T, Komine M, Yoshikawa R, Manabe K, Shiratori S (2017) Droplet motion control on dynamically hydrophobic patterned surfaces as multifunctional liquid manipulators. ACS Appl Mater Interfaces 9(12):10371–10377
13. Liu Y, Yao W, Yin X, Wang H, Han Z, Ren L (2016) Controlling wettability for improved corrosion inhibition on magnesium alloy as biomedical implant materials. Adv Mater Interfaces 3(8):1500723
14. Xu C, Zhang S, Chuang C, Miller E, Schwehr K, Santschi P (2011) Chemical composition and relative hydrophobicity of microbial exopolymeric substances (EPS) isolated by anion exchange chromatography and their actinide-binding affinities. Mar Chem 126(1–4):27–36
15. Latrache H, El GA, Karroua M, Hakkou A, Ait MH, El BA, Bourlioux P (2002) Relations between hydrophobicity tested by three methods and surface chemical composition of Escherichia coli. New Microbiol 25(1):75–82
16. Ferraz MP, Monteiro FJ, Serro AP, Saramago B, Gibson IR, Santos JD (2001) Effect of chemical composition on hydrophobicity and zeta potential of plasma sprayed HA/CaO-P2O5 glass coatings. Biomaterials 22(23):3105–3112
17. Asl AM, Kameli P, Ranjbar M, Salamati H, Jannesari M (2005) Correlations between microstructure and hydrophobicity properties of pulsed laser deposited diamond-like carbon films. Superlattices And Microstructures 81:64–79
18. Jia J, Fan J, Xu B, Dong H (2013) Microstructure and properties of the super-hydrophobic films fabricated on magnesium alloys. Journal Of Alloys And Compounds 554:142–146
19. Li S, Li H, Wang X, Song Y, Liu Y, Jiang L, Zhu D (2002) Super-hydrophobicity of large-area honeycomb-like aligned carbon nanotubes. J Phys Chem B 106(36):9274–9276
20. Feng L, Zhang Y, Cao Y, Ye X, Jiang L (2011) The effect of surface microstructures and surface compositions on the wettabilities of flower petals. Soft Matter 7(6):2977–2980
21. Wang X, Xu T, de Andrade MJ, Rampalli I, Cao D, Haque M, Roy S, Baughman RH, Lu H (2021) The interfacial shear strength of carbon nanotube sheet modified carbon fiber composites. Challenges in mechanics of time dependent materials 2:25–32
22. Cao D, Malakooti S, Kulkarni VN, Ren Y, Lu H (2021) Nanoindentation measurement of core-skin interphase viscoelastic properties in a sandwich glass composite. Mechanics of time-dependent materials 25:353–63
23. Cao D, Malakooti S, Kulkarni VN, Ren Y, Liu Y, Nie X, Qian D, Griffith DT, Lu H (2022) The effect of resin uptake on the flexural properties of compression molded sandwich composites. Wind Energy 25(1):71–93
24. Ishizaki T, Hieda J, Saito N, Saito N, Takai O (2010) Corrosion resistance and chemical stability of super-hydrophobic film deposited on magnesium alloy AZ31 by microwave plasma-enhanced chemical vapor deposition. Electrochim Acta 55(23):7094–7101
25. Rafieian F, Hosseini M, Jonoobi M, Yu Q (2018) Development of hydrophobic nanocellulose-based aerogel via chemical vapor deposition for oil separation for water treatment. Cellulose 25(8):4695–4710
26. Şakalak H, Yılmaz K, Gürsoy M, Karaman M (2020) Roll-to roll initiated chemical vapor deposition of super hydrophobic thin films on large-scale flexible substrates. Chem Eng Sci 215:115466
27. Luo BH, Shum PW, Zhou ZF, Li KY (2010) Preparation of hydrophobic surface on steel by patterning using laser ablation process. Surface And Coatings Technology 204(8):1180-1185

28. Khan A, Wang Z, Sheikh MA, Whitehead DJ, Li L (2011) Laser micro/nano patterning of hydrophobic surface by contact particle lens array. Appl Surf Sci 258(2):774–779
29. Nasser J, Lin J, Zhang L, Sodano HA (2020) Laser induced graphene printing of spatially controlled super-hydrophobic/hydrophilic surfaces. Carbon 162:570–578
30. Yang Z, Liu X, Tian Y (2020) Novel metal-organic super-hydrophobic surface fabricated by nanosecond laser irradiation in solution. Colloids And Surfaces A: Physicochemical And Engineering Aspects 587:124343
31. Kang B, Hyeon J, So H (2020) Facile microfabrication of 3-dimensional (3D) hydrophobic polymer surfaces using 3D printing technology. Appl Surf Sci 499:143733
32. Kang B, Sung J, So H (2021) Realization of superhydrophobic surfaces based on three-dimensional printing technology. International Journal Of Precision Engineering And Manufacturing-Green Technology 8:47–55
33. Sung J, Lee HM, Yoon GH, Bae S, So H (2023) One-step fabrication of superhydrophobic surfaces with wettability gradient using three-dimensional printing. International Journal Of Precision Engineering And Manufacturing-Green Technology 10(1):85–96
34. Garaigordobil A, Ansola R, Veguería E, Fernandez I (2019) Overhang constraint for topology optimization of self-supported compliant mechanisms considering additive manufacturing. Comput Aided Des 109:33–48
35. Kiener L, Saudan H, Cosandier F, Perruchoud G, Ummel A, Pejchal V, Zaltron P, Puyol Y, Lichtenberger M (2021) Compliant mechanism based on additive manufacturing. CEAS Space Journal 1–17
36. Chen CM, Yang S (2014) Directed water shedding on high-aspect-ratio shape memory polymer micropillar arrays. Adv Mater 26(8):1283–1288
37. Tayel SA, Abu El-Maaty AE, Mostafa EM, Elsaadawi YF (2022) Enhance the performance of photovoltaic solar panels by a self-cleaning and hydrophobic nanocoating. Sci Rep 12(1):21236
38. Nazhirah SN, Ghoshal SK, Arifin R, Hamzah K (2020) Titania nanoparticles activated tellurite zinc-silicate glass with controlled hydrophobic and hydrophilic traits for self-cleaning applications. J Non-Cryst Solids 530:119778
39. Zhu B, Zhang X, Zhang H, Liang J, Zang H, Li H, Wang R (2020) Design of compliant mechanisms using continuum topology optimization: a review. Mechanism And Machine Theory 143:103622
40. Liu M, Zhan J, Zhu B, Zhang X (2020) Topology optimization of compliant mechanism considering actual output displacement using adaptive output spring stiffness. Mechanism And Machine Theory 146:103728